Chapter-3

Framework structured $Ce_2(C_2O_4)_3.10H_2O$ as a Pseudocapacitive electrode of Hybrid Supercapacitor (HSC) for Large Scale Energy Storage Applications

3.1 Introduction

Metal-organic frameworks (MOFs) are interesting open framework structure where materials are constructed by joining metal-containing units with organic linkers, using strong bonds with permanent porosity [1]. Highly porous metal oxalate frameworks show battery-type faradaic pseudocapacitive characteristics. A reversible surface redox/ ion intercalation reaction mechanism was observed for charge storage on a material containing an active redox couple for charge transfer [2-10].

In this work, we have successfully synthesized the hydrated $Ce_2(C_2O_4)_3.10H_2O$. An electrochemical study was done in an aqueous electrolyte for pseudocapacitor applications. Porous $Ce_2(C_2O_4)_3.10H_2O$ were synthesized by single step process, after co-precipitation, synthesized power was dried at 80^{o}C for 3 hrs. The specific capacity value was 78mAh/g (Capacitance: 401 F/g) at 1A/g for porous anhydrous $Ce_2(C_2O_4)_3.10H_2O$ electrode in an aqueous 2M KOH electrolyte. Further, Aqueous asymmetric supercapacitors (ASCs) were fabricated; where porous $Ce_2(C_2O_4)_3.10H_2O$ is made as a positive electrode and Activated Carbon (AC) as a negative electrode. The highest specific energy is 96.5 Wh/kg and the specific power is ~ 750 W/kg at 1 A/g, by the combination of porous anhydrous $Ce_2(C_2O_4)_3.10H_2O$ and AC with high cyclic stability. Synthesis, characterizations and detailed electrochemistry of the developed porous $Ce_2(C_2O_4)_3.10H_2O$ electrode are presented in this manuscript.

3.2 Experimental Procedure

3.2.1 Synthesis

Synthesis of highly porous $Ce_2(C_2O_4)_3.10H_2O$ was done by precipitation method. $Ce(NO_3)_3.6H_2O$ was dissolved in 200ml of deionized water with continuous stirring at a

hot plate magnetic stirrer and 1.27g oxalic acid dehydrate ($H_2C_2O_4.2H_2O$) was added stoichiometry in solution. The entire mixture was stirred vigorously at 80ºC for 3h. After 3h of stirring white color precipitate of product $Ce_2(C_2O_4)_3.10H_2O$ was obtained. The obtained product is then washed several times with deionized water. Finally, the washed product $Ce_2(C_2O_4)_3.10H_2O$ was dried in a hot air oven at 90ºC overnight. The formation of Cerous Oxalate is presented below by equation 3.1.

$$Ce(NO_3)_3.6H_2O + H_2C_2O_4.2H2O \rightarrow Ce_2(C_2O_4)_3.10H_2O\downarrow + 2HNO_3 + 2H_2O \quad (3.1)$$

3.2.2 Characterizations

The crystal structure and phase purity of synthesized products were characterized through RigakuMiniflex desktop X-ray Diffractometer (XRD) with Cu-Ka radiation (λ= 0.154nm) in the 2θ range equal to 5º–50º with a step size of 0.02º. Xpert High Score (PANanylytical) software was used to identify the required phase. FE-SEM (FP 5022/22) was used to determine the surface morphology and structure of the sample. Infrared spectra of the samples were recorded using a Nicolet iS5 FTIR spectrometer in the range of 400 to 4000 cm^{-1}. Pore size distribution and specific surface area of the sample were measured by BET (MicrotracBEL). All electrochemical performances of the sample including CV, GCD, and EIS were conducted using a conventional three-electrode arrangement and were measured by Metrohm Autolab (PGSTAT204) equipped with a FRA32M module. Electrochemical measurements were analyzed using NOVA1.1 software.

3.2.3 Preparation of Electrode

Hydrated $Ce_2(C_2O_4)_3.10H_2O$ working electrodes were prepared 7:2:1 ratio of active material, activated carbon, and binder (PVDF) in NMP solvent. The homogenous slurry was prepared in mortar and slurry (~1mg) was cast over a $1cm^2$ area of Toray carbon paper. The coated electrode was dried at 80ºC for 12hrs.

3.3 Results and Discussion

XRD pattern of the powder sample gives conformation of the single-phase formation of $Ce_2(C_2O_4)_3.10H_2O$. **Fig. 3.1-a** shows the Rietveld refined XRD pattern of the prepared sample over the range of 2θ range of 5-50° with step size 0.02 º. The diffraction peaks appear at 7.4, 12.9, 16.59, 17.35, and 24.6° in the black curve, corresponding to the (110), (-110), (011), (-111), and (120) planes of $Ce_2(C_2O_4)_3.10H_2O$ (JCPDS file no.20-0268) respectively in monoclinic phase (space group: P21/c No- 14) with Lattice parameter a (Å) = 11.3470, b (Å) = 9.6300, c (Å) = 10.3920 α=γ 90º, β=114.5° [11-12]. **Fig. 3.1-b** shows the VESTA image of the $Ce_2(C_2O_4)_3.10H_2O$ power sample. Thermo-gravimetric analysis (TGA) as shown in **Fig. 3.1-c** was used to quantify the amount of monoclinic $Ce_2(C_2O_4)_3.10H_2O$. The first weight loss occurred between 100ºC-165ºC, which corresponds to the removal of structural water. TGA curve confirms the weight loss of 29% as 10 moles of water get removed from the sample in between this temperature range. Similarly, the second weight loss step occurs between the temperature range 244–304ºC in which weight loss of 32% was observed due to the decomposition of $Ce_2(C_2O_4)_3$. The weight losses can be represented as:

$$Ce_2(C_2O_4)_3.10H_2O \rightarrow Ce_2(C_2O_4)_3 + 2H_2O \text{ (above T~110 ºC)} \quad (3.2)$$

$$Ce_2(C_2O_4)_3 \rightarrow 2CeO_2 + 4CO_2 + 2CO \text{ (above T~ 300 ºC)} \quad (3.3)$$

Fig. 3.1-d shows the comparative XRD profile of intermediate phase $Ce_2(C_2O_4)_3.10H_2O$ and CeO_2 phase prepared after the TGA study. $Ce_2(C_2O_4)_3.10H_2O$ precipitates in monoclinic phase (space group: P21/c No- 14) whereas CeO_2 synthesized in a face-centered cubic lattice (space group: Fm3m (225), (JCPDS no. 34-0394).

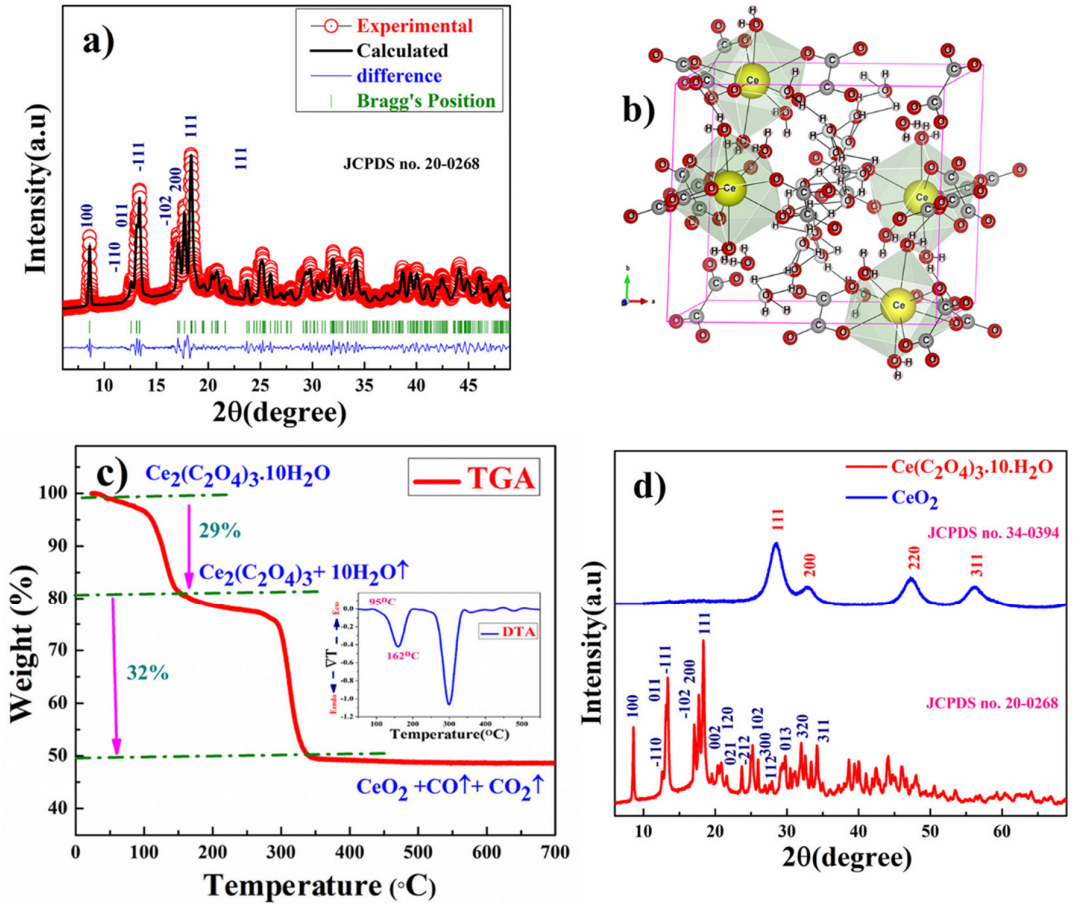

Figure 3.1 (a) *Rietveld refined XRD profile of $Ce_2(C_2O_4)_3.10H_2O$,* ***(b)*** *VESTA image of $Ce_2(C_2O_4)_3.10H_2O$* ***(c)*** *TGA of $Ce_2(C_2O_4)_3.10H_2O$ in an N_2 atmosphere (inset shows the DTA plot) and* ***(d)*** *comparative XRD profile of $Ce_2(C_2O_4)_3.10H_2O$ and final CeO_2 phase obtained after TGA study.*

FTIR spectrums of $Ce_2(C_2O_4)_3.10H_2O$ powder samples are shown in **Fig. 3.2-a** revealing the presence of different functional groups at different wavenumbers(cm^{-1}). The broad peak at 3347.05 cm^{-1} is ascribed to the stretching vibration of the hydroxyl group (-OH/H_2O) which signifies the presence of water in the compound. The observed peak at 1620.75 cm^{-1} was assigned for the anti-symmetric carbonyl stretching band (C=O) specific to the oxalate group. Two weak peaks at 1363.73 cm^{-1} and 1316.61 cm^{-1} were attributed to vibrations of $C_2O_4^{-2}$ (C–O) + (C–C) and (C–O) + (O–C=O), respectively. The peak at 794.77 cm^{-1} was assigned to the vibration mode of $C2O4^{-2}$, O–C=O bending vibrations

(O–C=O). The absorption peak at 492.05 cm^{-1} can be referred to combine Ce-O bonding present in the prepared sample of $Ce_2(C_2O_4)_3.10H_2O$ [13].

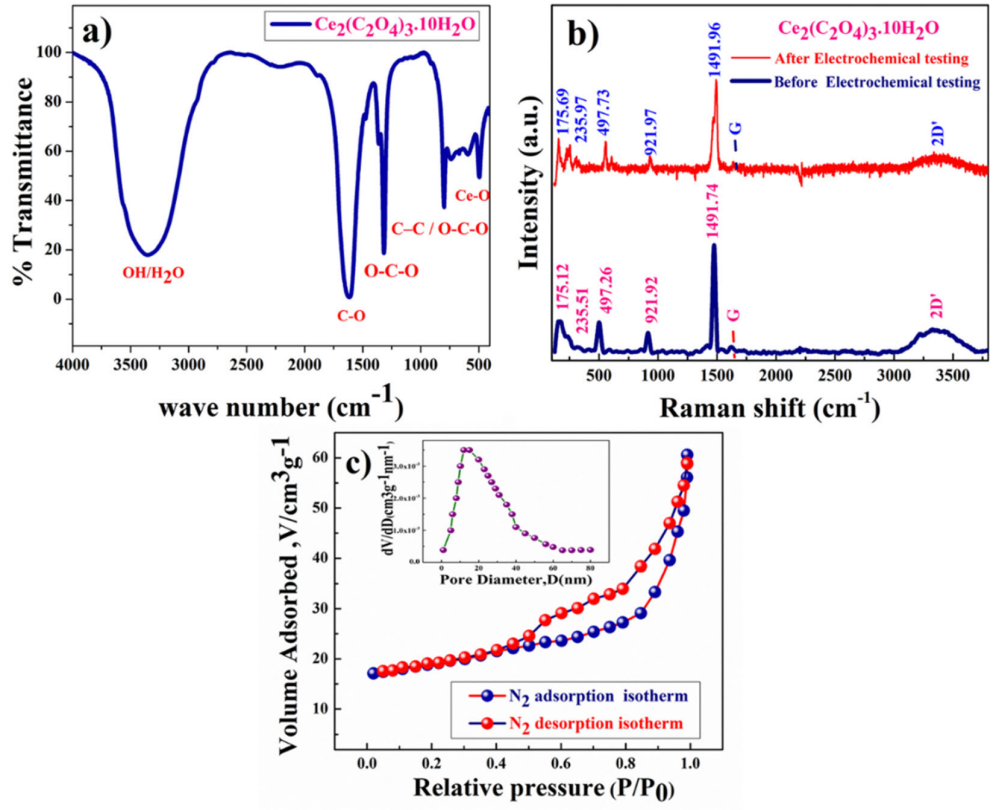

Figure 3.2 (a) *FT-IR spectra of $Ce_2(C_2O_4)_3.10H_2O$,* ***(b)*** *FT-Raman spectra of $Ce_2(C_2O_4)_3.10H_2O$ before and after electrochemical testing, and* ***(c)*** *BET surface area measurement plot of $Ce_2(C_2O_4)_3.10H_2O$*

A comparative FT-Raman study of $Ce_2(C_2O_4)_3.10H_2O$ powder was carried out and presented in **Fig. 3.2-b** which shows the FT-Raman spectra of $Ce_2(C_2O_4)_3.10H_2O$ before and after electrochemical testing. 175.69 cm^{-1} and 235.51 cm^{-1} represent the corresponding Ce-O symmetry stretching. 327.70 cm^{-1} represents the corresponding Ce-O asymmetry stretching. One-phonon longitudinal optical (LO) mode was observed both in $Ce_2(C_2O_4)_3.10H_2O$ powder in different frequency regions. LO mode was observed in $Ce_2(C_2O_4)_3.10H_2O$ powder at 497.26 cm^{-1}. The combined one-phonon longitudinal and one-phonon optical (LO + TO) mode was observed at 921.92 cm^{-1} for $Ce_2(C_2O_4)_3.10H_2O$ powder. The high-intensity peak at 1491.74 cm^{-1} is associated with a two-magnon (2 M)

band that arises from the Ce^{3+}- O^{2-}—Ce^{3+} vibration confirming the existence of $Ce_2(C_2O_4)_3.10H_2O$ phase. The Raman bands were observed both at 1624.6 cm^{-1} for $Ce_2(C_2O_4)_3.10H_2O$ and it corresponds to the G band that arises due to the C-C bond stretching vibration in the graphitic plane. Symmetrical stretching in the carboxylic functional group second-order disorder peaks 2D' appeared at 3357.9 cm^{-1} in $Ce_2(C_2O_4)_3.10H_2O$ sample. Thus FT-Raman study confirms the effective formation of $Ce_2(C_2O_4)_3.10H_2O$ [10, 13-14].

Fig. 3.2-c represents the BET results of the $Ce_2(C_2O_4)_3.10H_2O$ sample. The nitrogen adsorption and desorption isotherm show characteristics which are corresponding to the mesoporous structure for the cerium oxalate $Ce_2(C_2O_4)_3.10H_2O$ sample. The calculated BET-specific surface area and average pore diameter are 54.37 m^2/g and both micropores and mesopores with diameters of 1.72 to 4.58 nm, respectively. Mesopore structures attribute excellent electrochemical reactions due to high porosity. The calculated mesopores diameter of the $Ce_2(C_2O_4)_3.10H_2O$ sample is much bigger than the ions present in aqueous electrolytes.

HR-SEM image of the powder sample is shown in **Fig. 3.3-a**. The shape and morphology of the $Ce_2(C_2O_4)_3.10H_2O$ powder sample are columnar arrangements. EDX (Energy Dispersive X-ray Analysis) result that represents the elemental analysis of $Ce_2(C_2O_4)_3.10H_2O$ is shown in **Fig. 3.3-b**. **Fig. 3.3-(c-e)** shows the elemental distribution of Ce, C, and O in the sample respectively. software) of this region, confirming the crystalline nature of the sample.

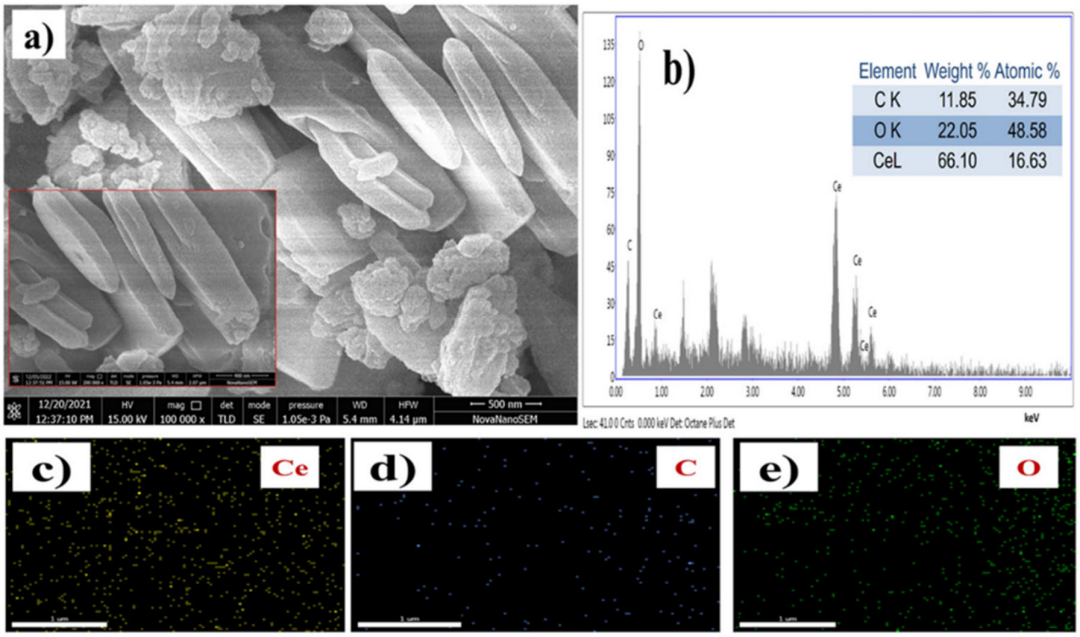

***Figure 3.3**. **(a)** HR-SEM image showing columnar shaped morphology of $Ce_2(C_2O_4)_3.10H_2O$ powder, **(b)** shows the EDX image of $Ce_2(C_2O_4)_3.10H_2O$ and **(c-e)** shows the elemental distribution of Ce, C, and O respectively in the sample.*

HR-TEM shows atomic arrangements at localized regions within materials of $Ce_2(C_2O_4)_3.10H_2O$ in **Fig. 3.4-a**. Columnar shape crystallites are present in the sample, and Lattice fringes are clearly visible in the inverse fast Fourier transform (FFT) (mapping with Gatan Digital micrograph HR-TEM shows atomic arrangements at localized regions within materials of $Ce_2(C_2O_4)_3.10H_2O$ in **Fig. 3.4-a**. Columnar shape crystallites are present in the sample, and Lattice fringes are clearly visible in the inverse fast Fourier transform (FFT) (mapping with Gatan Digital micrograph software) of this region, confirming the crystalline nature of the sample. **Fig. 3.4-a (i-iii)** represents FFT (Fast Furrier Transformation) and inverse FFT. **Fig. 3.4-b** shows the Interplanar distance, the d spacing value was found to be 0.663 nm of (-111) plane (calculate using Gatan Digital micrograph software). The lattice fringe spacing is in agreement with the interplanar spacing obtained from the XRD studies.

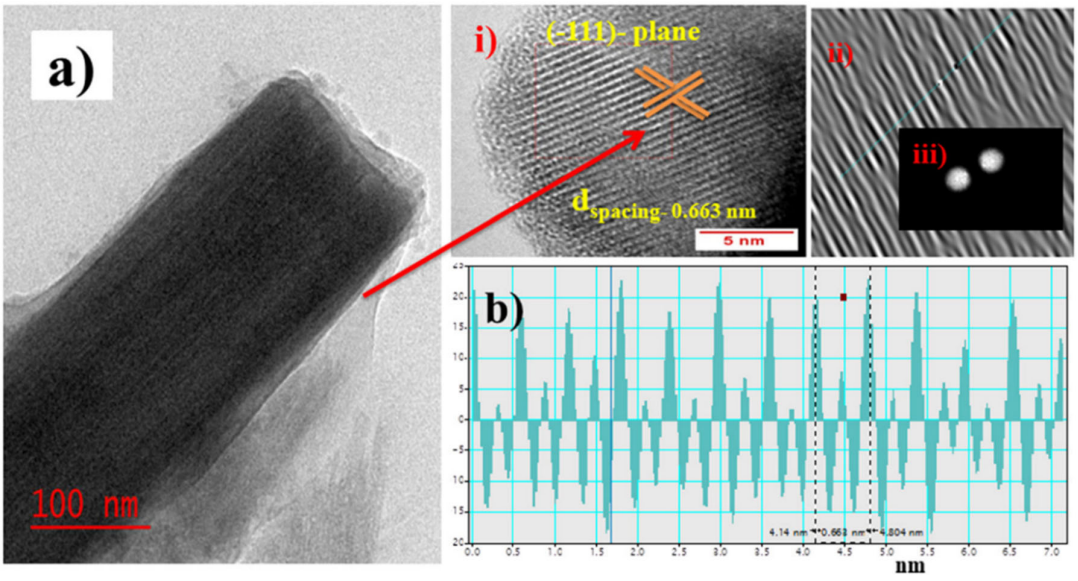

***Figure 3.4**. **(a)** HR-TEM image at localized regions **(i)** lattice fringes shows with **(ii)** FFT and **(iii)** inverse FFT of (-111) plane showing d spacing (0.663 nm) of porous $Ce_2(C_2O_4)_3.10H_2O$ and **(b)** shows calculated d spacing (0.663 nm) of (-111) plane (using gatan software).*

Fig. 3.5-a shows the X-ray photoelectron spectroscopy (XPS) survey of the $Ce_2(C_2O_4)_3.10H_2O$ sample, further confirming the presence of Ce. In the Ce3d spectrum shown in **Fig. 3.5-b**, four main peaks corresponding to spin-orbit split $3d_{5/2}$ and $3d_{3/2}$ appear in Ce3d(III) spectrum. The highest binding energy peaks at 885.59 eV and 904.65 eV present the final state of Ce $3d^9 4f^1$ O $2p^6$, and the lowest binding energy states located at 882.44 and 900.99 eV, respectively, are the results of Ce of the $3d^9 4f^2$ O $2p^5$ state [15-16]. The C1s spectrum shown in **Fig. 3.5-c** represents the C-C/C=C type carbon (C1s) binding energy at 284.22 eV, and binding energies for C-O and C=O type carbon (C1s) at 285.16 eV and 288.34eV respectively**.** The High-resolution O1s XPS spectrum is shown in **Fig. 3.5-d**. The predominant peaks at binding energies of 531.15, 531.8, and 532.7 eV are associated with C–O, C=O, and lattice H_2O type oxygen (O1s) respectively [5, 8-9].

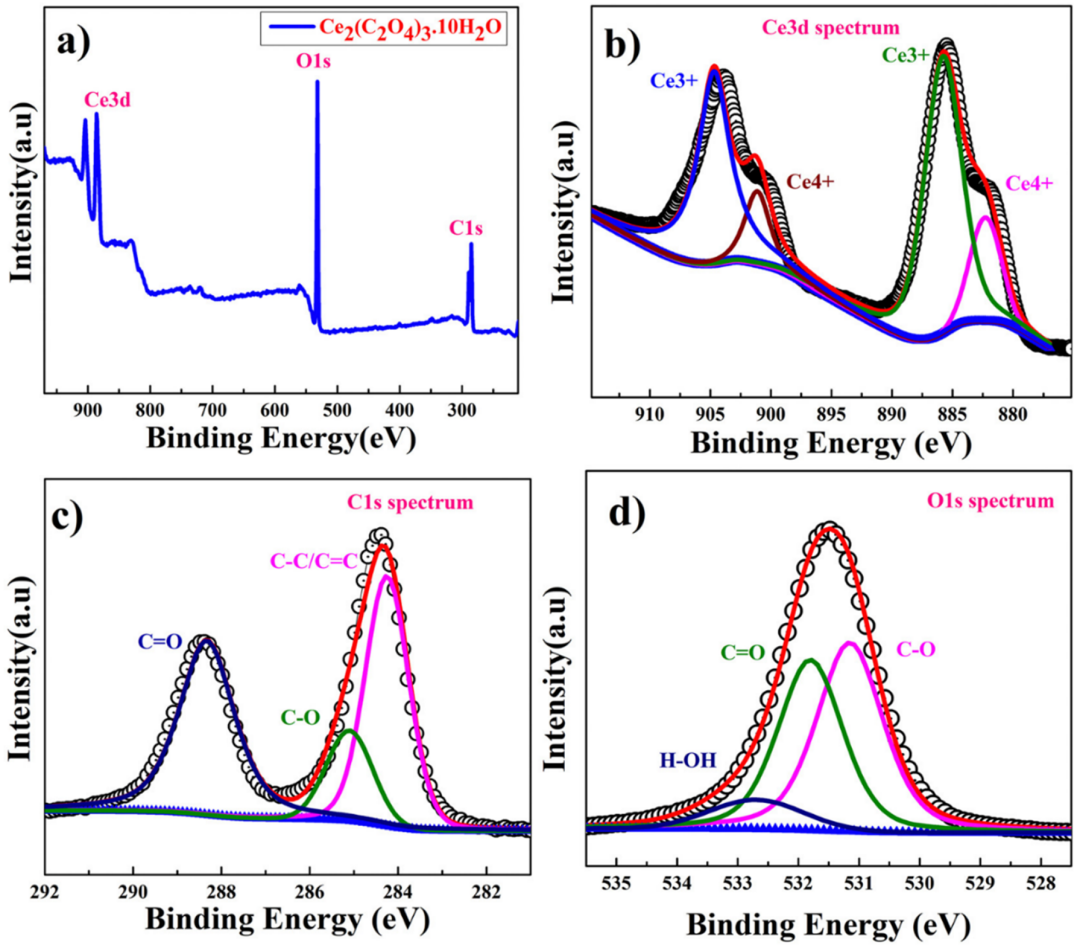

***Figure 3.5**. XPS plot of $Ce_2(C_2O_4)_3.10H_2O$; (a) full survey, (b) Ce(3d) spectrum, (c) C(1s) spectrum, and (d) O (1s) spectrum*

3.3.1 Electrochemical Studies

All Electrochemical tests were performed in 2M KOH electrolyte, where cerous Oxalte ($Ce_2(C_2O_4)_3.10H_2O$) and CeO_2 obtained from the TGA studies of the Cerous Oxalate were utilized as working electrodes, using a three-electrode system, where saturated Hg/HgO (1M KOH) is used as a reference electrode, and a Platinum wire is used as the counter electrode. Cyclic-voltammetry (CV) curve is performed in between the potential range of -0.3 V to 0.5 V for half-cell. **Fig. 3.6-a** shows a comparative Cyclic voltammetry plot for $Ce_2(C_2O_4)_3.10H_2O$ and CeO_2 phase at 5mV/s. **Fig. 3.6-b** represents the CV curve of $Ce_2(C_2O_4)_3.10H_2O$, nature of the curve suggests pseudocapacitive charge storage behavior utilizing surface redox (electrosorption) through diffusion-controlled intercalative storage

coupled with surface redox. Redox peaks originated due to the reversible transformation between Ce^{3+} to Ce^{4+} through Electrosorption (redox) of OH^- ion.

$$Ce_2(III)(C_2O_4)_3.10H_2O+2OH^-_{so} \longleftrightarrow Ce(IV)(OH^-)C_2O_4.2H_2O+2e^- \quad (3.4)$$

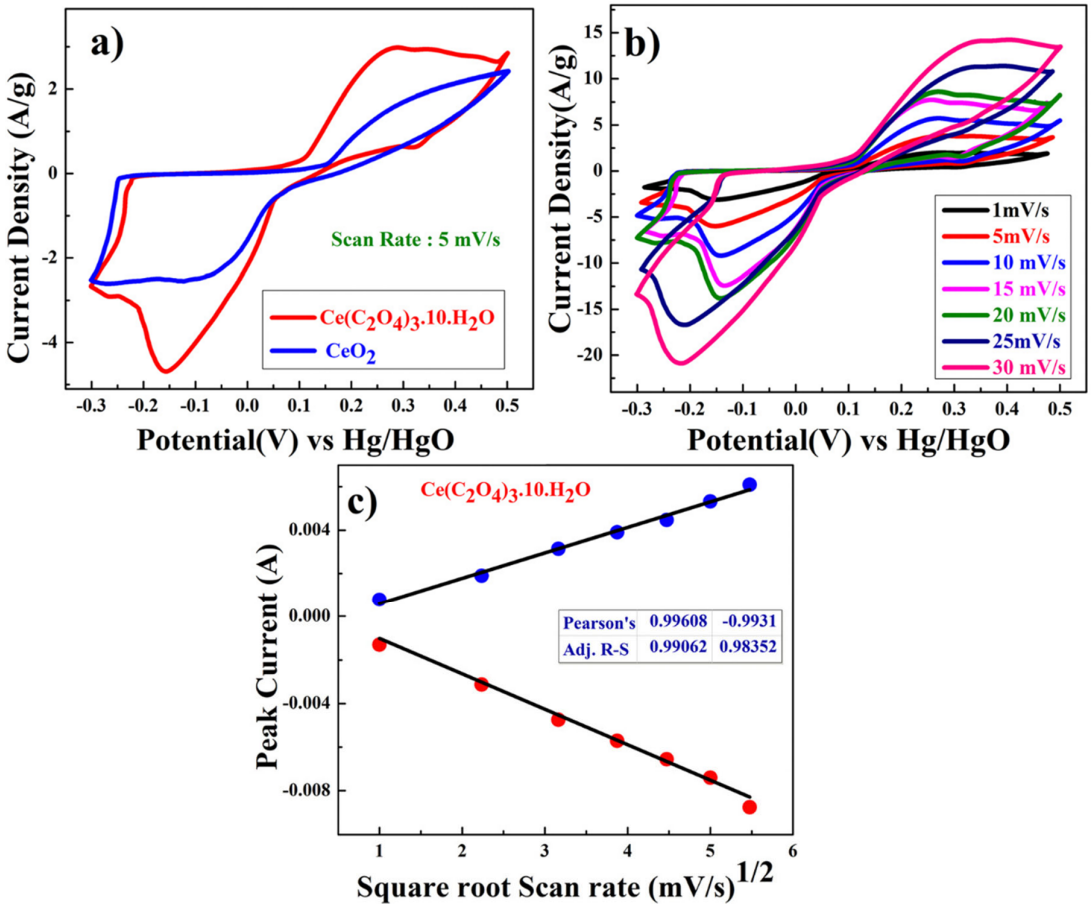

Figure 3.6: *(a) Comparative Cyclic voltammetry plot of $Ce_2(C_2O_4)_3.10H_2O$ and CeO_2 phase obtained after TGA study of the Oxalate, (b) Cyclic voltammetry plot of $Ce_2(C_2O_4)_3.10H_2O$ at different scan rate and (c) plot of log (peak current) vs square root of the scan rate for porous $Ce_2(C_2O_4)_3.10H_2O$ electrode.*

From the CV curve, specific capacitance C (F/g) can also be calculated using Eq.3.5 as one of the significant parameters to understand the electrochemical performance of the working electrode [17].

$$Csp = \frac{\int i\,(V)dV}{mV\vartheta} \quad (3.5)$$

The specific capacity C (mAh/g) can also be calculated by modifying Eq. 3.5.

$$C\left(\frac{mAh}{g}\right) = Csp * \Delta V = \frac{\int i\,(V)dV}{m\vartheta * 3.6} \quad (3.6)$$

Where 'm' is the mass of active material in the electrode (g), 'V' is the potential window (V), and 'ϑ' is the scan rate (mV/s).

The specific capacity of $Ce_2(C_2O_4)_3.10H_2O$ and CeO_2 was calculated using Eq. 3.6 and capacity were found 52 mAh/g (Capacitance: 278 F/g) and 15.73 mAh/g (Capacitance: 70.8 F/g) at 1mV/s. **Fig. 3.6-c** shows the linear relation between anodic and cathodic peak current with respect to the square root of scan rate, indicating that $Ce_2(C_2O_4)_3.10H_2O$ exhibits a semi-infinite diffusion-controlled process. Furthermore, the kinetics of the redox reaction of the electrode can be understood by determining the diffusion coefficient. The diffusion coefficient for the electrode was determined using Randles-Sevick equation [18].

$$i_p = 2.686 \times 10^5 \times n^{3/2} A D^{1/2} C_o v^{1/2} \quad (3.7)$$

Where i_p is peak current (A), n is the number of electrons transferred in the redox event (usually 1), A is electrode area in cm^2, D is diffusion coefficient in cm^2/s, C_o is OH^- ion concentration in mol/cm^3, ν is scan rate in V/s.

The diffusion coefficient of OH^- for the $Ce_2(C_2O_4)_3.10H_2O$ electrode was found to be 0.416×10^{-11} cm^2/s for oxidation and 1.8931×10^{-11} cm^2/s for the reduction reaction. Further to qualitatively understand the electrochemical kinetics of different charge storage properties of the electrode, the Power-law equation given below was utilized.

$$\boldsymbol{i = a\nu^b} \quad (3.8)$$

where a and b are adjustable values, i is the current (A), and ν is the scan rate (V/s). The value of b lies between 0.5 to 1, b= 0.5 stands for the semi-infinite diffusion-controlled reaction i.e. battery-type material, while b = 1 stands for the surface control reaction. **Fig. 3.7-a** shows the slopes (b value) of the corresponding log (peak current(i_p) vs log (v) plots. The b-value of oxidative and reductive currents were found to be 0.569 and 0.555 respectively, indicating the dominance of semi-infinite diffusion-controlled processes for these battery-type supercapacitors materials during the electrochemical reaction [19].

Fig. 3.7b shows Voltammetry sweep rate dependence to distinguish quantitatively the capacitive contribution to the current response. The current response at a fixed potential is the combination of two separate mechanisms, surface capacitive effects and diffusion-controlled insertion.

$$\boldsymbol{i(v) = k_1 v + k_2 v^{\frac{1}{2}}} \qquad (3.9)$$

For more understanding Eq. 3.9 was modified

$$\frac{\boldsymbol{i(v)}}{\boldsymbol{v^{\frac{1}{2}}}} = \frac{\boldsymbol{k_1}}{\boldsymbol{v^{\frac{1}{2}}}} + \boldsymbol{k_2} \qquad (3.10)$$

From Eq. 3.10 $k_1\nu$ and $k_2\ \nu^{1/2}$ explain the current contributions from the surface capacitive effects and the diffusion-controlled intercalation process, respectively. Thus, after the determination of k_1 and k_2, we can be able to quantify, the fraction of the current due to each of these contributions at specific potentials.

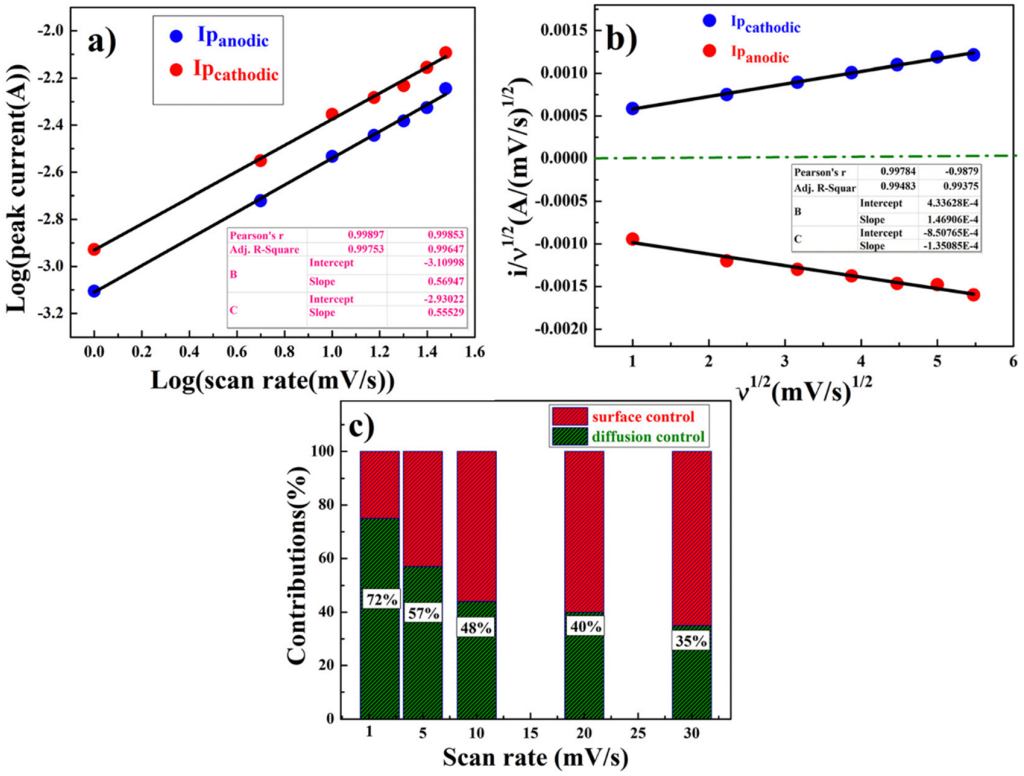

Figure 3.7: *Electrodynamic characteristics of the $Ce_2(C_2O_4)_3.10H_2O$ electrode; (a) b value plot of the linear relationship between log (peak current) and log (scan rate) at two different scan rate regions, (b) plot of the power law of the charged state at a potential and discharged state at a potential, (c) contribution of diffusive and capacitive contribution at different scan rates*

Linear fitting of the curve was carried out to determine the k_1 and k_2 values from the slope and intercept of the y-axis. The representative curve of $i(V)/\nu^{1/2}$ vs. $\nu^{1/2}$ in **Fig. 3.7-b** represent the contribution of surface capacitance and diffusion-controlled interaction process at different scan rate in **Fig. 3.7-c**. In **Fig. 3.7-c,** after determining the k1 and k2 values, here represent the contribution of surface capacitance (52 %) and diffusion-controlled interaction (48 %) at peak potential at 0.317 V at scan rate 10mV/s.

Galvanostatic charge/discharge experiments were performed for a more accurate capacitance assessment of $Ce_2(C_2O_4)_3.10H_2O$ electrodes. From the charge-discharge curve, the specific capacitance of the electrode can be calculated using the equation mentioned below:

$$\boldsymbol{Csp} = \frac{\boldsymbol{I\Delta t}}{\boldsymbol{m\Delta V}} \tag{3.11}$$

The specific capacity of the electrode can be calculated by modifying the Eq. 3.11 as represented below.

$$\boldsymbol{C}\left(\frac{\boldsymbol{mAh}}{\boldsymbol{g}}\right) = \boldsymbol{Csp} * \boldsymbol{\Delta V} = \frac{\boldsymbol{I\Delta t}}{\boldsymbol{m}*\boldsymbol{3.6}} \tag{3.12}$$

Where I is the discharge current (A), Δt the discharge time (s), m is the mass of the active material in the electrode (g) and ΔV is the potential change during discharge (V).

Fig. 3.8-a shows a comparative Charge/discharge (GCD) curve of $Ce_2(C_2O_4)_3.10H_2O$ and CeO_2 electrodes at a 1A/g current rate. Specific capacity $Ce_2(C_2O_4)_3.10H_2O$ and CeO_2 electrode were found 78mAh/g (Capacitance: 401 F/g) and 23 mAh/g (Capacitance: 103.5 F/g). **Fig. 3.8-b** depicts that the specific capacity $Ce_2(C_2O_4)_3.10H_2O$ are 78mAh/g (Capacitance: 401 F/g), 37mAh/g (Capacitance:190 F/g), 26 mAh/g (Capacitance: 133 F/g) and 15mAh/g (Capacitance: 77.2 F/g) at current densities of 1, 2, 3 and 5A/g respectively. It has been observed that with an increase in current density, there was a decrement in specific capacitance. **Fig. 3.8-c** shows the capacitance of highly porous $Ce_2(C_2O_4)_3.10H_2O$ electrode with cycle numbers at different constant current rates.

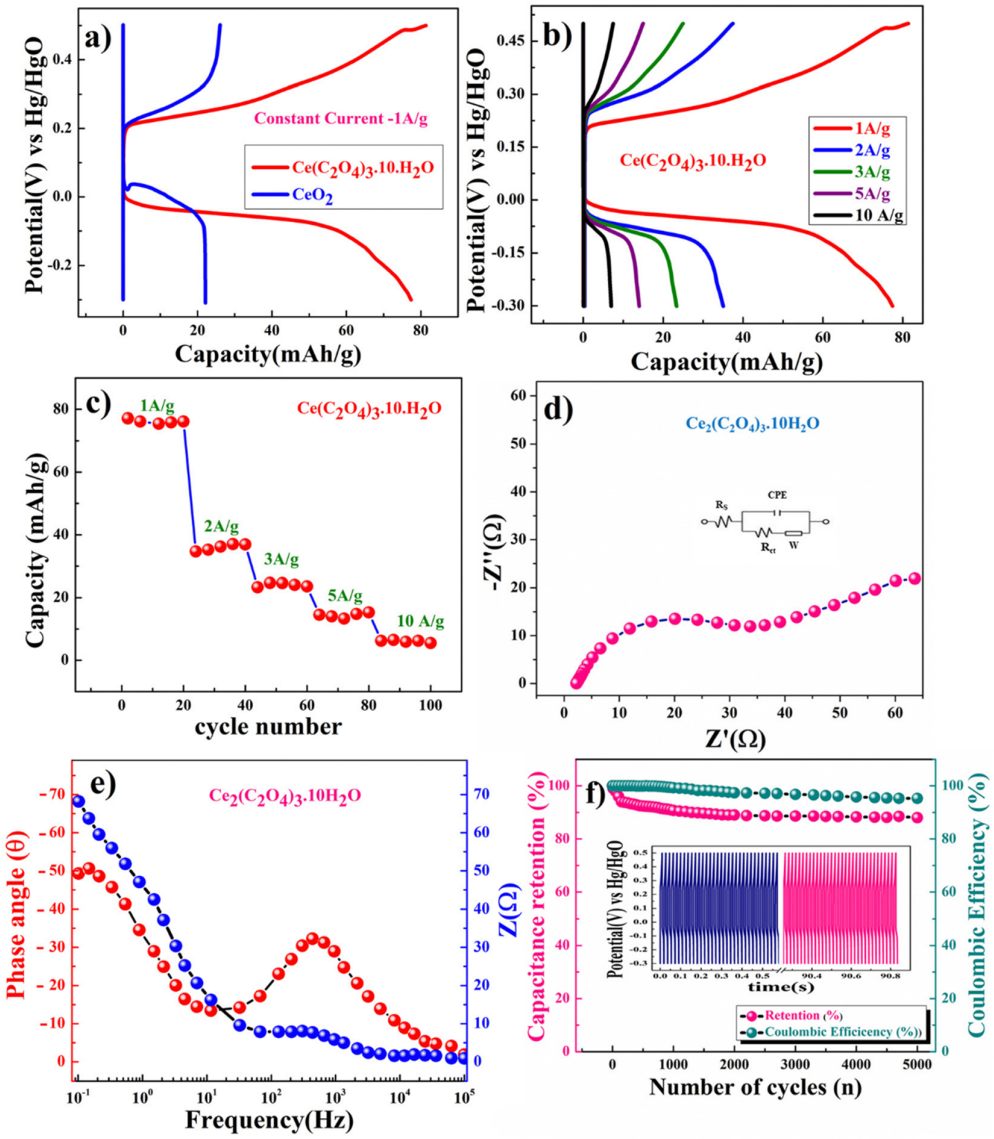

Figure 3.8. *(a) Comparative Charge/discharge curve of battery type $Ce_2(C_2O_4)_3.10H_2O$ and CeO_2 at 1A/g (b) Charge/discharge curve of battery type $Ce_2(C_2O_4)_3.10H_2O$ with different constant current (c) capacity performance of $Ce_2(C_2O_4)_3.10H_2O$ at different constant current rates, and (d) EIS Nyquist plot and (e) EIS Bode plot of $Ce_2(C_2O_4)_3.10H_2O$ electrode at 10 mV (AC) between 0.1 Hz and 100 kHz and (f) Capacitance retention and Coulombic efficiency porous $Ce_2(C_2O_4)_3.10H_2O$ with 5000 cycles*

In addition to electrochemical stability, we performed data AC electrochemical impedance spectroscopy (EIS) as shown in Nyquist Plot at 10mV in **Fig. 3.8-d** in the frequency range of 100kHz-0.1Hz. The specific impedance contribution is mainly attributed to the impedance distributions over electric series resistance (Rs), charge transfer resistance (Rct), and Warburg impedance (Rw). Higher frequency resistance for $Ce_2(C_2O_4)_3.10H_2O$

electrodes, the intercept of the EIS spectra on the real axis was at 2.36 Ω, indicating very small internal resistance. Lower frequency data represent the Warburg diffusion resistance for samples. The slope of the straight line of porous $Ce_2(C_2O_4)_3.10H_2O$ electrode in the low-frequency region is close to a 45° angle (very close to –Z″(Ω) axis) from the horizontal line represents the characteristic of more battery type or diffusion-controlled capacitance behavior of the $Ce_2(C_2O_4)_3.10H_2O$ electrode. This also represents fast OH^- ion diffusion in the porous structure of the electrode [20].

Bode plot representations of phase angle (φ) as a function of frequency that can be used to visualize the relative contributions of capacitive and resistive elements as it suggests ideal capacitance behavior at φ = 90° and ideal battery type behavior at φ = 45° The Bode plot shown in **Fig. 3.8-e** illustrates the phase angle of the $Ce_2(C_2O_4)_3.10H_2O$ electrode with respect to the applied frequency between 100 kHz to 0.1Hz. The phase angle of the $Ce_2(C_2O_4)_3.10H_2O$ electrode was found to be 49.5° which suggests the predominant battery-type charge storage behavior. **Fig. 3.8-f** exhibits excellent long-term cycle stability of highly porous anhydrous $Ce_2(C_2O_4)_3.10H_2O$ electrodes at the current rate of 10A/g for 5000 cycles. It was observed that 87 % of capacity retention after 5000 cycles indicates that specific capacitance wasn't changed after long cycling and shows the applicability of framework structure to make robust electrodes. Simultaneously, the plot also displays superior coulombic efficiency ($\eta = {}^{t_d}/_{t_c}$) of electrode close to 95.3 % after 5000 cycles of charge/discharge which reveals the high reversibility of the $Ce_2(C_2O_4)_3.10H_2O$ electrode.

3.3.2 Two electrode tests in Full cell Hybrid supercapacitor mode:

To understand the real charge storage behavior or applicability of porous $Ce_2(C_2O_4)_3.10H_2O$ sample relative to AC (Activated carbon), two electrode measurements have been conducted in 2M KOH. To determine the maximum performance of the cell

during the full test, the storage capacity of positive and negative electrode need to be balanced as per the following equation given below:

$$\frac{1}{C_{total}} = \frac{1}{C_{positive}} + \frac{1}{C_{negative}} \quad (3.13)$$

For balancing the charge storage capacity of the cell, the mass ratio (m^+/m^-) of positive and negative electrode material was estimated using the following equation:

$$\frac{m^+}{m^-} = \frac{C_- \times \Delta E_-}{C_+ \times \Delta E_+} \quad (3.14)$$

$m^+, m^-, C_+, C_-, \Delta E_+, \Delta E_-$ are mass, specific capacitance, and potential window of positive and negative electrodes estimated by three-electrode measurement.

Fig. 3.9-a shows the respective CV curves for AC (activate carbon) and porous $Ce_2(C_2O_4)_3.10H_2O$ positive electrodes at a 10 mV/s scan rate. The calculated mass ratio ($\frac{m^+}{m^-}$) was kept 1:1.2 for the asymmetric cell, weight of the positive material was 2.12 mg (active material, $Ce_2(C_2O_4)_3.10H_2O$ (1.48 mg): acetylene black (0.42mg): PVDF (0.22 mg) and mass of negative electrode (activate carbon) is 2.38 mg, resulting overall cell mass equal to 4.49 mg. **Fig. 3.9-b** demonstrates the CV curve of porous $Ce_2(C_2O_4)_3.10H_2O$ //AC cell in two electrodes in ASCs mode at the scan rate of 1mV/s to 100mV/s in the operating potential window of 1.5V. **Fig. 3.9-c** subsequently, shows the galvanostatic charge/discharge profile conducted for measuring the actual capacity of the cell. The cell`s capacitance was calculated using Eq. 3.12 and values are found to be 129mAh/g (Capacitance: 309F/g), 77 mAh/g (Capacitance: 184 F/g), 51 mAh/g (Capacitance:122 F/g), 30 mAh/g (Capacitance: 72 F/g), and15 mAh/g (Capacitance: 36 F/g) at the current densities of 1A/g, 2A/g, 3A/g,5A/g and 10A/g respectively. In **Fig. 3.9-d,** the EIS plot (Nyquist) is shown in the frequency range of 1MHz to 0.1Hz at the scan rate of 10mV/s shows higher charge transformation resulting in higher capacitance for the full cell ($Ce_2(C_2O_4)_3.10H_2O$ //AC). The impedance distributions over electric series resistance (Rs),

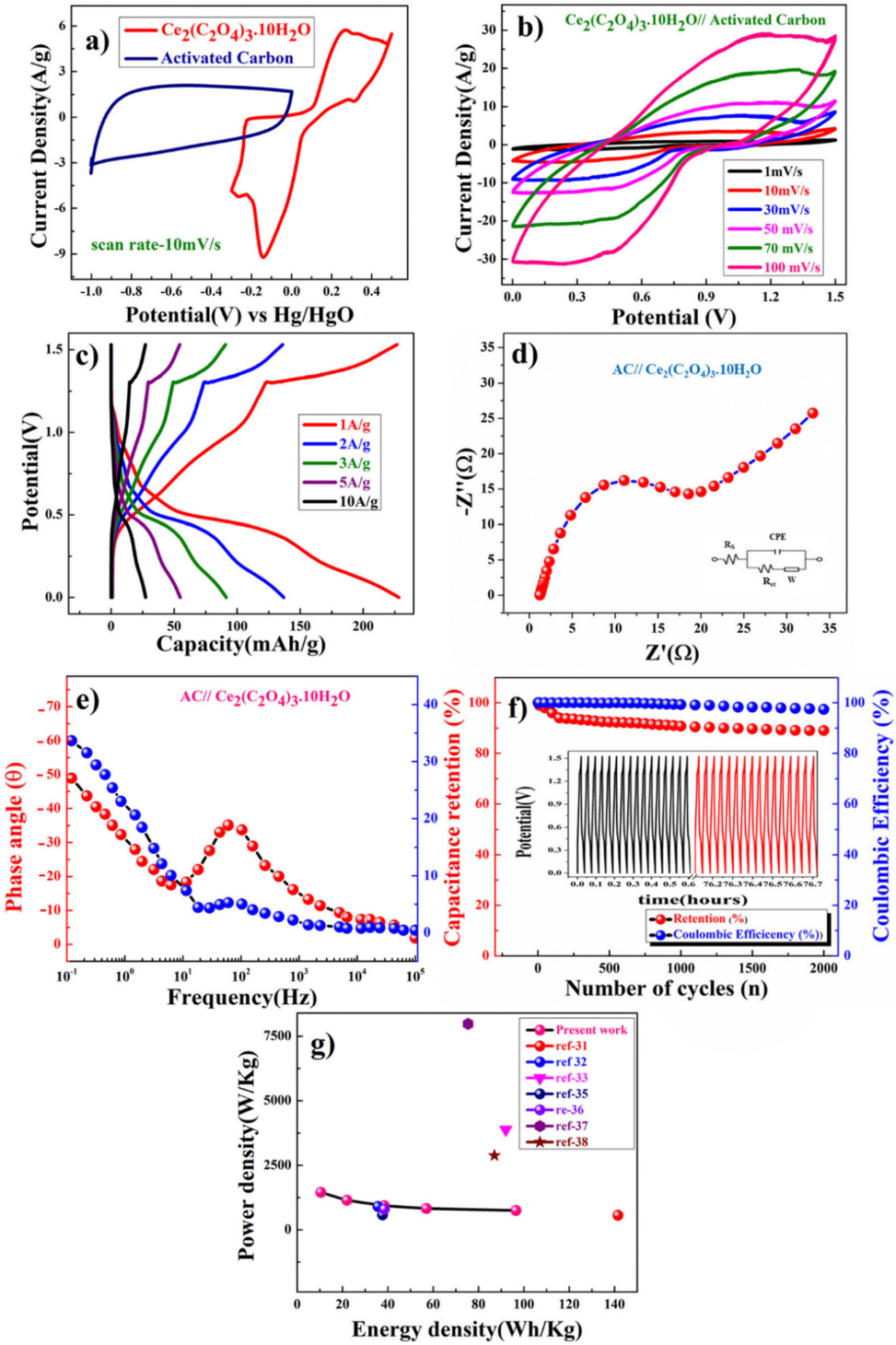

Figure 3.9. *(a) Respective CV curves for activated carbon (AC) and porous $Ce_2(C_2O_4)_3.10H_2O$ at 10 mV/s, (b) plot for Activated carbon // Porous $Ce_2(C_2O_4)_3.10H_2O$ cell in ASC mode CV at different scan rates, (c) charge/discharge at different current rates of Activated carbon // Porous $Ce_2(C_2O_4)_3.10H_2O$ (d) EIS at 10 mV (AC), (e) EIS Bode plot of AC// $Ce_2(C_2O_4)_3.10H_2O$ cell at 10 mV (AC), (f) Capacitance retention and coulombic efficiency, and (g) comparative Ragone plot (power density vs. energy density) with two electrode cells((AC// $Ce_2(C_2O_4)_3.10H_2O$) in Hybrid supercapacitor mode.*

charge transfer resistance (Rct), and Warburg impedance (Rw) were made; Higher frequency resistance and the intercept of the EIS spectra on the real axis were found to be 6.2 Ω and 16.4 Ω respectively indicating very small internal resistance for the $Ce_2(C_2O_4)_3.10H_2O$ electrode. Lower frequency data represent the Warburg diffusion resistance for samples and the slope of the straight line of porous $Ce_2(C_2O_4)_3.10H_2O$ electrode in the low-frequency region is close to 45° angle (very close to Z″(Ω) axis) from the horizontal line represents the characteristic of diffusion-controlled battery type charge storage behaviour of the porous $Ce_2(C_2O_4)_3.10H_2O$ electrode [15].

The Bode plot shown in **Fig. 3.9-e** illustrates the phase angle of the $Ce_2(C_2O_4)_3.10H_2O$ electrode with respect to the applied frequency between 100 kHz to 0.1Hz. The phase angle of the full cell (AC// Ce_2 $(C_2O_4)_3.10H_2O$) was found to be 50.09° which suggests battery type predominant charge storage mechanism in the full cell.

In **Fig. 3.9-f,** the plot shows the coulombic efficiency of two electrode full cells has lost only 4 % with higher capacity retention close to 92.6% of its initial value after 2000 cycles. Specific energy and specific power of asymmetric capacitors were calculated using the following equations:

$$\boldsymbol{E(Wh/kg) = \frac{1}{2}\frac{C_{ASCs}}{3.6}V^2} \qquad (3.15)$$

$$\boldsymbol{P(W/kg) = \frac{E*3600}{t_{dis}}} \qquad (3.16)$$

Where C_{ASCs} is specific capacitance, V is operating voltage and t_{dis} is discharge time [16].

Fig. 3.9-g shows the plot of specific energy vs specific power at different constant current rates. The cell results in the highest specific energy of 96.5 Wh/kg at 1 A/g current density with specific power reaching ~750 W/kg. Maximum specific power of ~1453W/kg was obtained when specific energy was reduced to ~10.58 Wh/kg at 10 A/g of the current density.

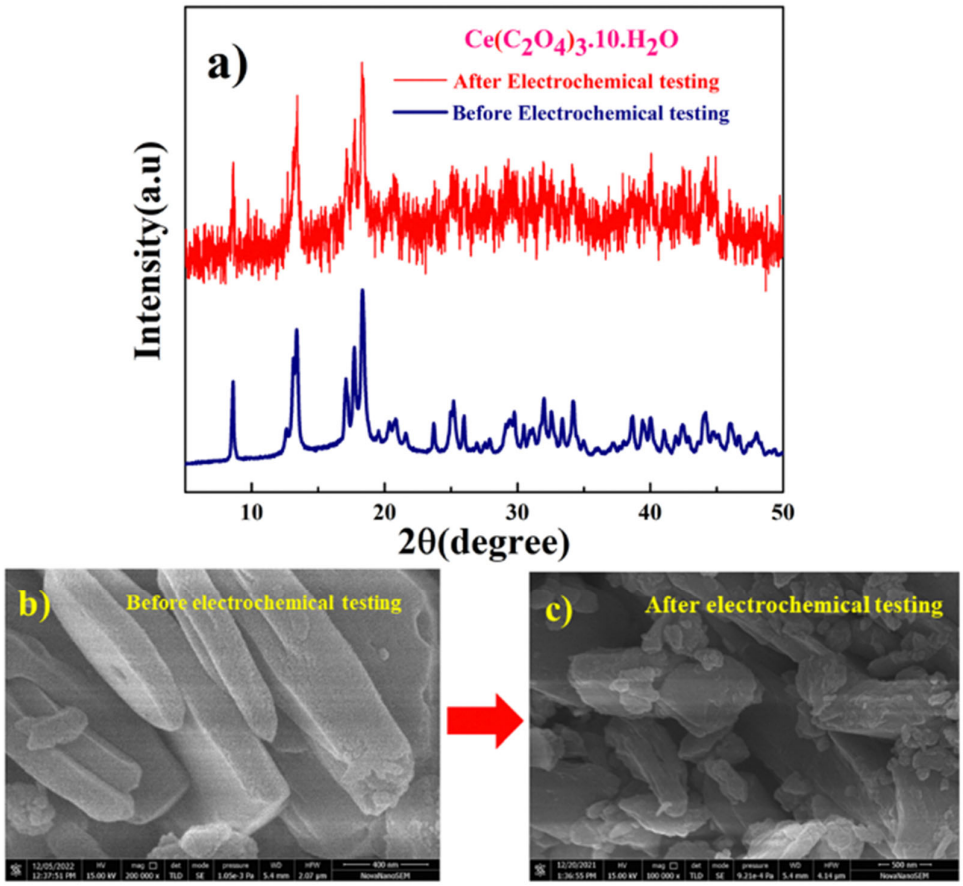

***Figure 3.10**. (a) A comparative XRD $Ce_2(C_2O_4)_3.10H_2O$ powder sample before and after the Electrochemical study, (b) A comparative HR-SEM study of $Ce_2(C_2O_4)_3.10H_2O$ powder sample before and after the Electrochemical study.*

Fig. 3.10-a shows a comparative XRD $Ce_2(C_2O_4)_3.10H_2O$ powder sample before and after the Electrochemical study, and similarly, **Fig. 3.10-b** shows the HR-SEM study of $Ce_2(C_2O_4)_3.10H_2O$ powder sample before and after Electrochemical study. Studies clearly show the stability of the electrode material after electrochemical tests. The robust oxalate framework structure results in the higher structural stabilities of the electrode which results in superior and robust charge storage properties of the electrode.

3.4 Conclusions

In summary, $Ce_2(C_2O_4)_3.10H_2O$ powder was successfully synthesized by co-precipitation method and was characterized by Powder XRD, SEM/HR-TEM, FT-IR, and Raman spectroscopy. The electrode showed diffusion-controlled pseudocapacitive charge storage

exhibiting a specific capacity of 78mAh/g (Capacitance: 401 F/g) at a current density of 1A/g and having excellent cyclic stability. Comparative performances of different metal-oxalate-based electrodes are summarised in **Table 3.1**.

Material	**Morphology**	**Capacitance** **(F g^{-1})**	**Operating Window (V)**	**Electrolyte**	**Reference**
$NiC_2O_4 \cdot 2H_2O$	Nanoflakes	990 F/g	0 to 0.45	2M KOH	[3]
NiC_2O_4	2D thin sheet	2835F/g at1 A/g	0 to 0.4	6M KOH	[4]
Anhydrous CoC_2O_4	Nanorods	2116 F/ g at 1 A/g	0 to 0.3	2M KOH	[5]
MnC_2O_4/GO	Olive-like	122 F/g at 0.5 A/g	-0.1 to 0.55	6M KOH	[6]
FeC_2O_4/rGO hydrogel	3D macro-micro-mesoporous	591 F/g at 2A/g	−1.3 to 0 V	1M Na_2SO_4	[7]
$Ni_{0.55}Co_{0.45}C_2O_4$	micro-cuboid	562 C/g at 1A/ g	0 to 0.6	6 M KOH	[8]
Anhydrous $Co_{0.5}Ni_{0.5}C_2O_4$	Nano flakes	2409 F/g at 1A/g	0 to 0.6	2M KOH	[9]
Anhydrous NiC_2O_4	QDs	1638F/g at 1A/g	0 to 0.5	2M KOH	[10]
$Ce_2(C_2O_4)_3.10H_2O$	**Columnar**	**401 F/g at 1A/g**	**-0.3 to 0.5**	**2M KOH**	**Present study**

***Table 3.1**: A comparative study of metal-oxalate-based electrode materials*

The predominant intercalative diffusion-controlled pseudocapacitive charge storage mechanism seems to be operative behind the high charge storage capacity of the electrode as a contribution for intercalative (diffusion-controlled) and surface-controlled charges stored by porous anhydrous $Ce_2(C_2O_4)_3.10H_2O$ were found to be 48 % and 52% respectively at 10 mV/s scan rate. Porous $Ce_2(C_2O_4)_3.10H_2O$ //AC full cell resulted in 96.5 Wh/kg of maximum specific energy with specific power equivalent to 750 W/kg in the voltage window of 1.5V in 2M KOH electrolyte at the current rate of 1A/g.These results confirm that porous $Ce_2(C_2O_4)_3.10H_2O$ electrode can be applied as a potential pseudo-capacitive electrode for large energy storage applications.

References

1. V. Aravindan, J. Gnanaraj, Y. S. Lee and S. Madhavi, Insertion-Type Electrodes for Nonaqueous Li-Ion Capacitors, Chem. Rev. 2014, 114, 11619−11635

2. M. Saraf, R. Rajak, and S. M. Mobin, A fascinating multitasking Cu-MOF/rGO hybrid for high performance supercapacitors and highly sensitive and selective electrochemical nitrite sensors *J. Mater. Chem. A*, 2016, **4**, 16432–16445.

3. N. K. Mishra, A. K. Singh, R. Mondal, P. Singh, $NiC_2O_4{\cdot}2H_2O$ Nanoflakes: A Novel Redox-mediated Intercalative Pseudocapacitive Electrode for Supercapacitor Applications in Aqueous KOH and Neutral Na_2SO_4 electrolytes, ChemestrySelect, **2022** 7 (21), e202201134.

4. C. Zhao, Y. Jiang, S. Liang, F. Gao, L. Xie, and L. Chen, Two-dimensional porous nickel oxalate thin sheets constructed by ultrathin nanosheets as electrode materials for high-performance aqueous supercapacitors. CrystEngComm, **2020**, 22, 2953.

5. N. K.Mishra, R. Mondal and P. Singh, Synthesis, characterizations and electrochemical performances of anhydrous CoC_2O_4 nanorods for pseudocapacitive energy storage applications, RSC Adv., **2021**, 11, 33926-33937.

6. T. Liu, G. Shao, M. Ji, and Z. Ma Composites of olive-like manganese oxalate on graphene sheets for supercapacitor electrodes Ionics, **2014**, 20 145–149.

7. W. Liu, Y. Song, H. Wang, H.-F. Wang and L. F. Yan, 3D macro-micro-mesoporous FeC2O4/ graphene hydrogel electrode for high performance 2.5 V aqueous asymmetric supercapacitors, Chinese J. Chem. Phys, 2018, 31 707–716.

8. L. Wang, R. Zhang, Y. Jiang, H. Tian, Y. Tan, K. Zhu, Z. Yu, and W. Li, Interfacial synthesis of micro-cuboid $Ni_{0.55}Co_{0.45}C_2O_4$ solid solution with enhanced electrochemical performance for hybrid supercapacitors. Nanoscale, **2019**, 11, 13894–13902.

9. N. K. Mishra, R. Mondal, T. Maiyalagan, and P. Singh, Synthesis, Characterizations, and Electrochemical Performances of Highly Porous, Anhydrous $Co_{0.5}Ni_{0.5}C_2O_4$ for Pseudocapacitive Energy Storage Applications, ACS Omega **2022**, 7, 2, 1975–1987.

10. R. Mondal, K. G. Nigam, N. K. Mishra, A. Gupta, and P. Singh, Intercalative pseudocapacitive anhydrous NiC_2O_4 quantum dot electrode for the fabrication of supercapacitor using aqueous KOH and neutral Na_2SO_4 electrolyte, Journal of Energy Storage, **2023**, 60, 106549.

11. A. Michaelides, S. Skoulika, and A. Aubry, Crystal growth and structure of $La_2(C_2O_4)_{3\ 9.5}H2O$, Materials Research Bulletin, **1988**, 23, 4, 579-585.

12. M. A. Gabal, A. K. Shabaan Elroby, and A. Y. Obaid, Synthesis and characterization of nano-sized ceria powder via oxalate decomposition route, Powder Technology, **2012**, 229, 112–118.

13. C. Tamain, B. Arab-Chapelet, M. Rivenet, X. F. Legoff, G. Loubert, S. Grandjean, and F. Abraham, Coordination Modes of Americium in the $Am_2(C_2O_4)_3(H_2O)_6{\cdot}4H_2O$ Oxalate: Synthesis, Crystal Structure, Spectroscopic Characterizations and Comparison in the $M_2(C_2O_4)_3(H_2O)_6{\cdot}nH_2O$ (M = Ln, An) Series, Inorg. Chem. **2016**, 55, 1, 51–61.

14. K. K. Sahu, R. K. Sahoo, L. D. Beshara, and M. Mohapatra, Facile synthesis of nickel oxalate@carbon as electrical double layer and its derived nickel oxide as pseudo-type supercapacitor electrodes, Ionics **2021**, 27:819–832.

15. H. B. Trinh, J.-C. Lee, S. Kim, and J. Kim, Recovery of Cerium from Spent Autocatalyst by Sulfatizing−Leaching−Precipitation Process, ACS Sustainable Chem. Eng. **2020**, 8, 15630−15639.

16. M. Kettnera, K. Ševčíková, P. Homola, V. Matolín, and V. Nehasil, Influence of the Ce–F interaction on cerium photoelectron spectra in CeOXFY layers, Chemical Physics Letters, 2015, 639, 126-130.

17. R. Mondal, N. K. Mishra, T. Maiyalagan, A. Gupta, and P. Singh, $La_{1-x}K_xFeO_{3-\delta}$: An Anion Intercalative Pseudocapacitive Electrode for Supercapacitor Application, ACS Omega, **2021**, 6, 45, 30488–3049.

18. A. Gupta, V. Kushwaha, R. Mondal, A. N. Singh, R. Prakash, K. D. Mandal and P. Singh, $SrFeO_{3-\delta}$: a novel $Fe^{4+} \leftrightarrow Fe^{2+}$ redox mediated pseudocapacitive electrode in aqueous electrolyte, Phys. Chem. Chem. Phys., **2022**, 24, 11066-11078.

19. V. Augustyn, J. Come, M. A. Lowe, J. W. Kim, P.-L. Taberna, S. H. Tolbert, H. D. Abruña, P. Simon, and B. Dunn, High-rate electrochemical energy storage through Li+ intercalation pseudocapacitance. Nat. Mater. **2013**, 12, 518– 522.

20. J. S. Ko, C.-H. Lai, J. W. Long, D. R. Rolison, B. Dunn, and J. N. Weker, Differentiating Double-layer, Psuedocapacitance, and Battery-like Mechanisms by Analyzing Impedance Measurements in Three Dimensions, ACS Appl. Mater. Interfaces 2020, 12, 12, 14071–14078.